Vol. 6 • No. 10 • May 25 • 2016
www.advenergymat.de

ADVANCED ENERGY MATERIALS

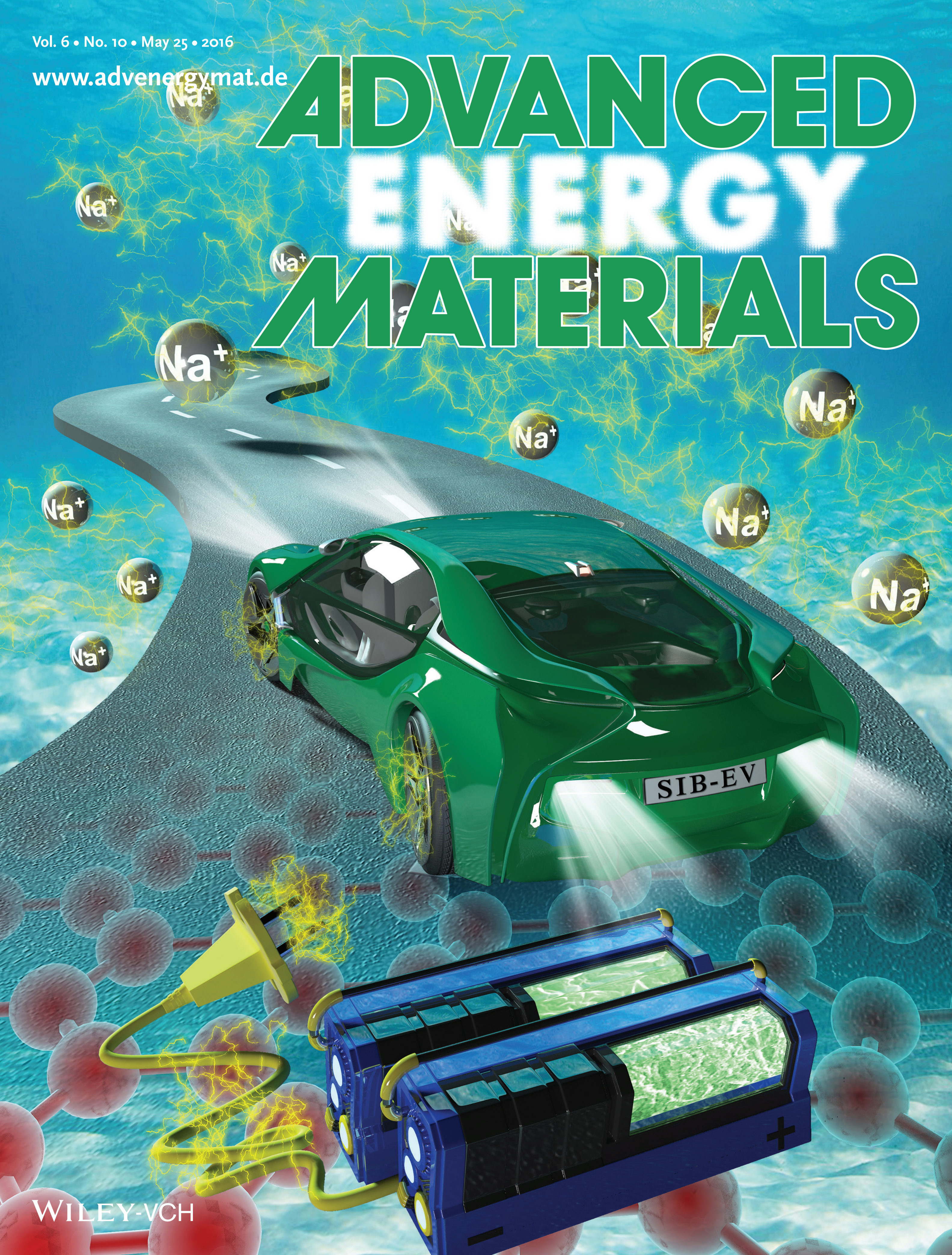

WILEY-VCH

Controlled SnO_2 Crystallinity Effectively Dominating Sodium Storage Performance

Linlin Fan, Xifei Li, Bo Yan, Jianmin Feng, Dongbin Xiong, Dejun Li, Lin Gu,* Yuren Wen, Stephen Lawes, and Xueliang Sun**

The exploration of sodium ion batteries (SIBs) is a profound challenge due to the rich sodium abundance and limited supply of lithium on earth. Here, amorphous SnO_2/graphene aerogel (a-SnO_2/GA) nanocomposites have been successfully synthesized via a hydrothermal method for use as anode materials in SIBs. The designed annealing process produces crystalline SnO_2/graphene aerogel (c-SnO_2/GA) nanocomposites. For the first time, the significant effects of SnO_2 crystallinity on sodium storage performance are studied in detail. Notably, a-SnO_2/GA is more effective than c-SnO_2/GA in overcoming electrode degradation from large volume changes associated with charge–discharge processes. Surprisingly, the amorphous SnO_2 delivers a high specific capacity of 380.2 mAh g^{-1} after 100 cycles at a current density of 50 mA g^{-1}, which is almost three times as much as for crystalline SnO_2 (138.6 mAh g^{-1}). The impressive electrochemical performance of amorphous SnO_2 can be attributed to the intrinsic isotropic nature, the enhanced Na^+ diffusion coefficient, and the strong interaction between amorphous SnO_2 and GA. In addition, amorphous SnO_2 particles with the smaller size better function to relieve the volume expansion/shrinkage. This study provides a significant research direction aiming to increase the electrochemical performance of the anode materials used in SIBs.

1. Introduction

Nowadays, lithium ion batteries (LIBs) are widely used in portable devices and even in electrical vehicles.[1] For these applications, undoubtedly, LIBs are one of the most efficient energy storage systems due to their long lifespan, high energy density, and environmental benignity.[2] However, as more demand emerges for electrical vehicles and hybrid electric vehicles, and as emphasis shifts to the power grid and other large-scale applications, LIBs have been heavily restricted by their high cost and the limited supply of lithium on earth.[3] To circumvent these problems, it is necessary to explore alternative battery systems to replace LIBs. Sodium ion batteries (SIBs) have tremendous potential because of the abundance and easy accessibility of sodium reserves, resulting in low material costs.[4] Practically, SIBs have attracted increasing attention for energy storage applications in renewable energy.[5]

The development of SIBs dates back to the late 1980s, in approximately the same time period as LIBs.[6] Normally, Li and Na have similar physical and chemical properties, including ionicity, electronegativity, and electrochemical activity. Thus, to some degree, the development of SIBs benefits from the well-established understanding of lithium-based electrochemical systems. Nevertheless, Na ions are about 55% larger in radius than Li ions, which results in some difficulties in finding a suitable host material to accommodate Na ions and allow reversible and rapid ion insertion and extraction.[7] Expanded graphite has been reported as a superior anode material in SIBs compared to regular graphite.[3] It has an increased interlayer lattice distance, yet retains a long-range-ordered layered structure analogous to graphite, allowing the Na ions to be reversibly inserted into and extracted from expanded graphite. This work provides a good strategy for SIB development. However, for new applications such as electric vehicles and large scale energy storage units, its low reversible capacity limits its use. Many researchers have made great efforts to explore electrode materials with higher energy density, such as $Li_4Ti_5O_{12}$,[5,8] TiO_2,[9] Fe_2O_3,[10] SnO_2,[11] MoS_2,[12] and Na_2FePO_4F,[7,13] which have been the focus of many experimental and theoretical studies. In this study, SnO_2 was targeted due to its appealing features of relatively high theoretical reversible capacity, low cost, abundance, ease of synthesis, and improved safety.[14] Therefore, SnO_2 is a promising high-capacity electrode material for SIBs. The sodiation and desodiation reactions can be described as follows

---

L. Fan, Prof. X. Li, B. Yan, Dr. J. Feng, D. Xiong,
Prof. D. Li, Prof. X. Sun
Energy and Materials Engineering Centre
College of Physics and Materials Science
Tianjin Normal University
Tianjin 300387, P. R. China
E-mail: xfli2011@hotmail.com; xsun9@uwo.ca

Prof. L. Gu, Y. Wen
Institute of Physics
Chinese Academy of Sciences
Beijing 100190, P. R. China
E-mail: l.gu@iphy.ac.cn

S. Lawes, Prof. X. Sun
Nanomaterials and Energy Lab
Department of Mechanical and Materials Engineering
Western University
London, Ontario N6A 5B9, Canada

DOI: 10.1002/aenm.201502057

$$SnO_2 + 4Na \rightarrow Sn + 2Na_2O \quad (1)$$

$$Sn + 3.75Na \leftrightarrow Na_{3.75}Sn(Na_{15}Sn_4) \quad (2)$$

Importantly, the extremely large volume expansion of ≈520% occurs during alloying from Sn to $Na_{15}Sn_4$,[15] along with the aggregation of Sn clusters upon cycling, which result in rapid capacity fading.[16] All of these factors severely restrict the practical application of SnO_2 in SIBs. Therefore, developing a facile, scalable approach to synthesize SnO_2 material with enhanced cycling stability and rate capabilities still remains a challenge.

Many research efforts have been devoted to solving the aforementioned challenges of SnO_2 anodes through the use of unique morphological design[17] and incorporation of carbon-based materials.[18] Graphene and its composites have been extensively investigated for SIBs due to its extraordinary electrical behavior, chemical stability, and high specific surface area (2630 m^2 g^{-1}).[15b,19] A large number of studies have focused on developing SnO_2/graphene nanocomposites using various methods, including hydrothermal methods[20] and wet-mechanochemical processes.[21] As previously reported by our group,[22] the existence of 2D graphene in the composites can largely relieve the volume expansion/contraction of SnO_2 nanoparticles. For instance, the designed ultrafine SnO_2 nanoparticles on reduced graphene oxide as SIB anode materials were reported to show a high reversible capacity of 330 mAh g^{-1} as well as a capacity retention of 81.3% after 150 cycles.[23] The recent study revealed that the introduction of nitrogen into graphene was beneficial to increasing the cycling performance and rate capability of SnO_2/graphene nanocomposites for SIBs.[24] Therefore, SnO_2 incorporated with graphene has been demonstrated to be one of the most promising anode materials for SIBs.

During the sodium storage process, SnO_2 anodes undergo large volume expansion/contraction, similar to lithium storage. In comparison to crystalline SnO_2, amorphous SnO_2 with intrinsically isotropic behavior may help reduce the degradation of the electrode associated with volume changes upon cycling. Our group has demonstrated that the crystallinity of the SnO_2 anode has an important influence on lithium storage performance.[25] Similarly, SnO_2 anodes with amorphous and crystalline phases may display totally different sodium storage behavior. However, the degree of crystallinity of the SnO_2 material is not easily controlled, and it is thus difficult to study the effects of SnO_2 crystallinity on sodium storage performance. So far, no study has been reported focusing on this important strategy.

Inspired by this, amorphous and crystalline SnO_2/graphene aerogel (marked as a-SnO_2/GA and c-SnO_2/GA) nanocomposites were successfully synthesized by a facile approach. Both materials were investigated as anode materials for SIBs. The a-SnO_2/GA significantly differs from c-SnO_2/GA in structure although both have similar composition. To the best of our knowledge, it is the first time the significant impact of SnO_2 crystallinity on SIB performance has been studied. This approach provides a new direction for addressing the challenges of rechargeable SIBs.

2. Results and Discussion

X-ray diffraction (XRD) and Raman spectroscopy were performed to measure the structural characteristics of the as-prepared products. The XRD patterns are shown in **Figure 1**a.

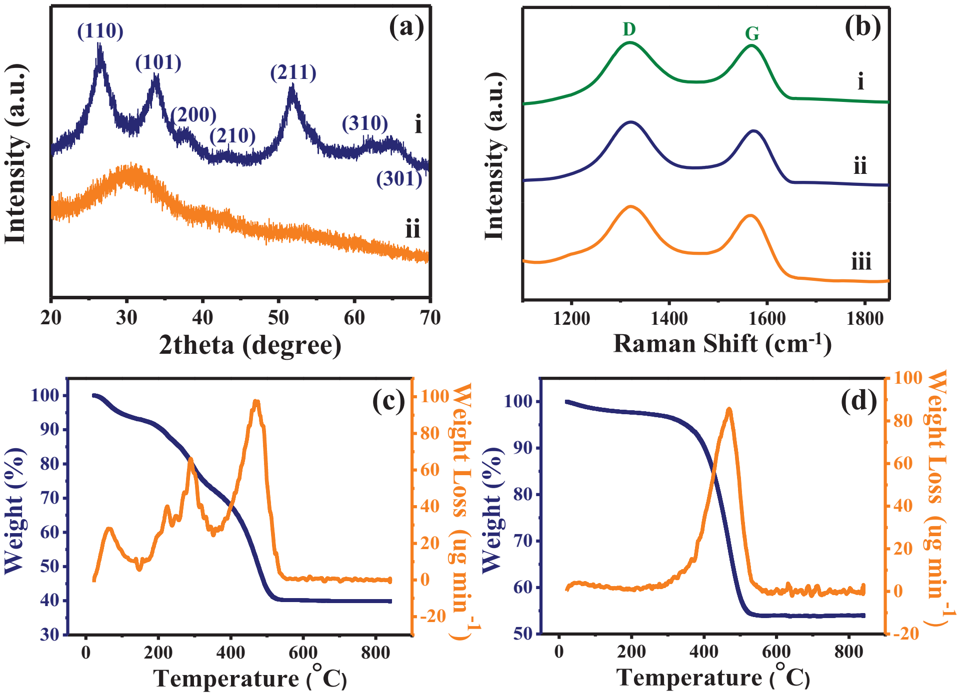

Figure 1. a) XRD patterns of (i) c-SnO_2/GA and (ii) a-SnO_2/GA; b) Raman spectra of (i) pristine GA, (ii) c-SnO_2/GA, and (iii) a-SnO_2/GA; TGA and DTG curves of (c) a-SnO_2/GA and (d) c-SnO_2/GA.

Similar to other reports of SnO_2-based composites,[26] the diffraction peaks of c-SnO_2/GA are clearly distinguishable, and are well-indexed to the rutile structure of SnO_2 (cassiterite, JCPDS No. 41–1445), indicating its high degree of crystallinity. The diffraction peaks observed at 26.6°, 33.9°, 37.9°, 42.6°, 51.8°, 61.9°, and 65.9° can be assigned to the (110), (101), (200), (210), (211), (310), and (301) planes of the rutile SnO_2 phase, respectively. By sharp contrast, no diffraction peaks of a-SnO_2/GA are detected except for the broad peak around 29.28–31.15°. This phenomenon confirms that amorphous SnO_2 was successfully formed in the a-SnO_2/GA.

Typical D and G bands were observed in the Raman spectra (Figure 1b) of the pristine GA, a-SnO_2/GA, and c-SnO_2/GA. The D band results from disorder in the symmetrical hexagonal graphitic lattice, while the G band originates from the in-plane stretching motion of symmetric sp^2 C—C bonds.[27] The I_D/I_G intensity ratio is a measure of the degree of disorder and average size of the sp^2 domains.[26b] It can be observed that the I_D/I_G ratios of pristine GA, a-SnO_2/GA, and c-SnO_2/GA are 1.46, 1.70, and 1.70, respectively. The increase in the ratio of I_D/I_G indicates a decrease in the size of the sp^2 carbon domains, due to the anchoring of SnO_2 quantum dots on the GA.[28] The weight percentages of SnO_2 in the as-prepared products were determined using thermogravimetric analysis (TGA). In the a-SnO_2/GA sample (Figure 1c), the peak at 64 °C is due to the removal of moisture and the two peaks at 229 and 289 °C correspond to the decomposition of oxygen-containing groups. These three peaks are not observed for the c-SnO_2/GA sample (Figure 1d), due to the annealing process. Both samples show a peak at 396 °C associated with the burning of GA in air. Consequently, the SnO_2 loadings of a-SnO_2/GA and c-SnO_2/GA are about 50.7% and 54.4%, respectively.

The chemical composition of a-SnO_2/GA and c-SnO_2/GA was carefully investigated via X-ray photoelectron spectroscopy (XPS). As described in **Figure 2**a, the full spectrum result shows the existence of C, O, and Sn in the SnO_2/GA, with no impurity peaks, which confirms the high purity of the composites. The C1s XPS was measured to check the changes in the chemical state of a-SnO_2/GA and c-SnO_2/GA. In Figure 2b, the Sn 3d 3/2 and Sn 3d 5/2 peaks depicted in the fine spectrum of Sn 3d confirm that the Sn atoms are in the form of SnO_2.[29] Figure 2c,d compared the C1s spectra of a-SnO_2/GA and c-SnO_2/GA. Obviously, the C1s peak of both SnO_2/GA can be resolved into four components: graphitized carbon (284.5 eV), carbon in C—O bonds (286.6 eV), carbonyl carbon (C=O, 287.6 eV), and carboxyl carbon (O—C=O, 288.9 eV).[30] Interestingly, the intensity of these oxygen-containing groups in the c-SnO_2/GA is lower than that of a-SnO_2/GA. The area percentage of the peaks in the C1s spectra of a-SnO_2/GA and c-SnO_2/GA are quantified, and the values are listed in Table S1 (Supporting Information). Obviously, the major bonding species are C—C. It is worthy to note that the total area percentage of oxygenated functionalities in a-SnO_2/GA and c-SnO_2/GA are estimated to be 35% and 19%, respectively. The decrease of oxygen-containing groups in c-SnO_2/GA confirms that the GA was further reduced upon annealing process. Furthermore, more information on surface functional group of the both SnO_2/GA was studied by FT-IR spectroscopy (Figure S1, Supporting Information). The absorption bands 1399–1064 cm^{-1} are ascribed to the C=O, the absorption bands at 1729 cm^{-1} are ascribed to the C=O stretching of —COOH, and the broader peak around 3407 cm^{-1} is assigned to hydroxyl groups.[31] Notably, compared to a-SnO_2/GA, the intensities of c-SnO_2/GA spectra associated with oxygen-containing groups decrease due

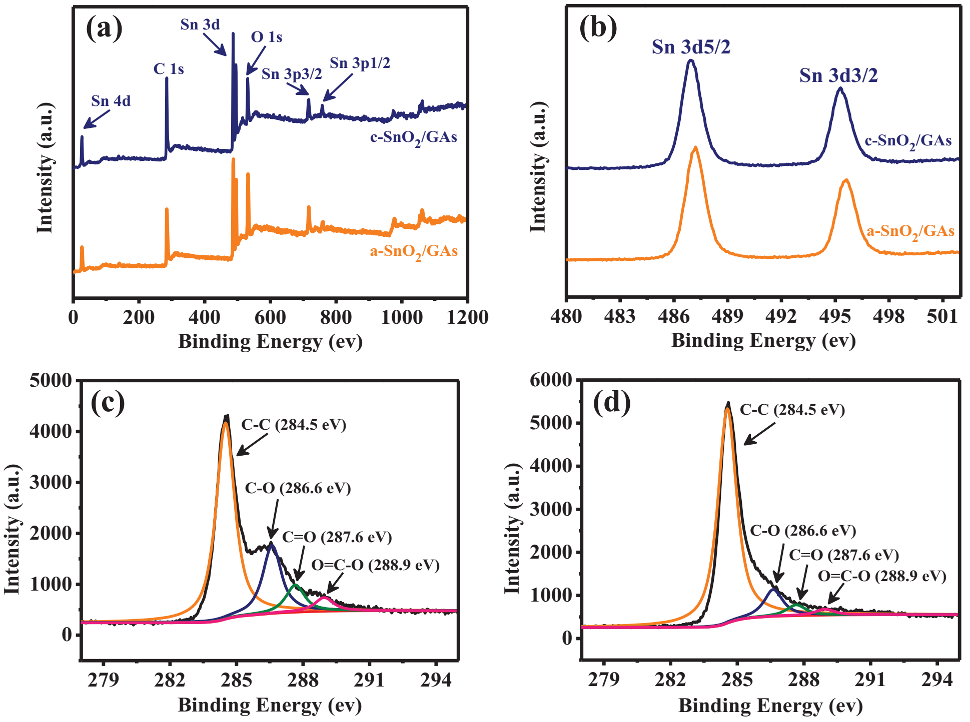

Figure 2. XPS analysis of a-SnO_2/GA and c-SnO_2/GA: a) the survey spectrum; b) Sn 3d spectra; C 1s spectra of (c) a-SnO_2/GA and (d) c-SnO_2/GA.

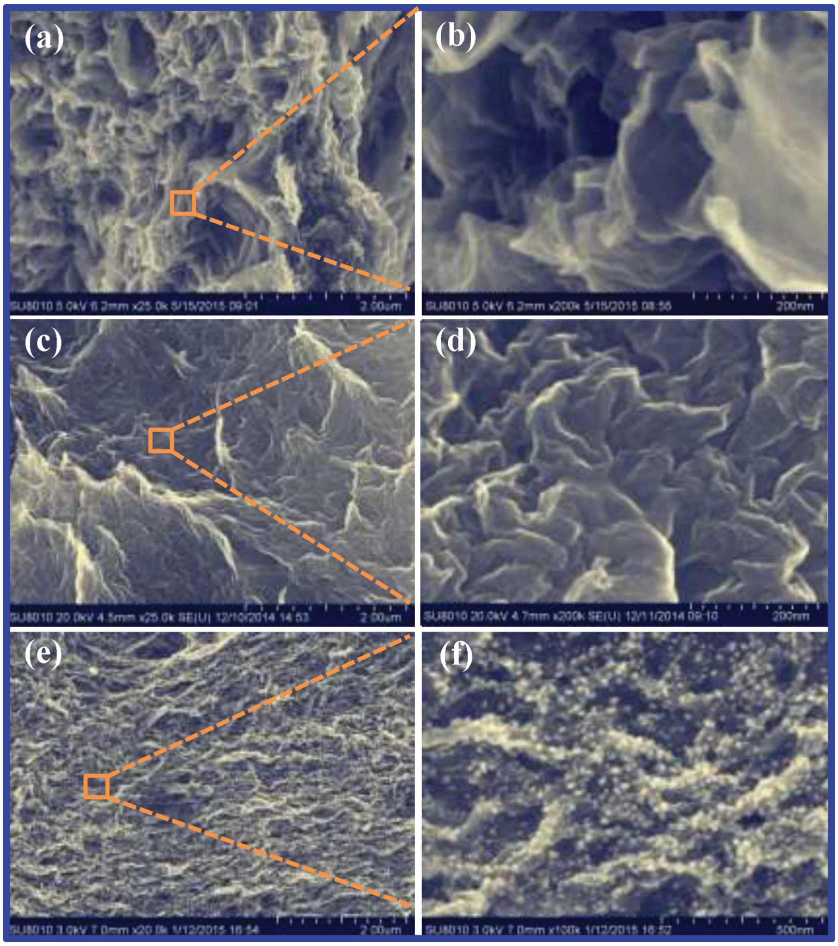

Figure 3. Typical SEM images of (a,b) pristine GA, (c,d) a-SnO_2/GA, and (e,f) c-SnO_2/GA.

to obvious loss of some functional groups during annealing process. This phenomenon may be ascribed to two factors: (a) the GA was further reduced during annealing; and (b) the stronger interaction between amorphous SnO_2 and GA. To further confirm the interaction between amorphous SnO_2 and GA, the crystalline SnO_2/GA-3 (see Figure S2a–e in the Supporting Information for the detailed information) were successfully obtained by extending the hydrothermal reaction time up to 3 h. Through carefully comparing the region related with oxygen-containing groups in Figure S2f (Supporting Information), it can be surmised that the bonding with strong interaction may be formed between amorphous SnO_2 and GA.[14c]

The morphological features of the synthesized products were investigated by scanning electron microscopy (SEM) and the results are shown in **Figure 3**. Pristine gossamer GA is presented in Figure 3a,b. Moreover, it can be seen that the average layer number of GA is 9 (see Figure S3, Supporting Information). The specific surface area was estimated to be around 345 m^2 g^{-1} based on the nitrogen adsorption–desorption analysis using the Brunauer–Emmett–Teller (BET) method. For both a-SnO_2/GA and c-SnO_2/GA, the low-magnification SEM images (Figure 3c,e) show that the SnO_2 nanoparticles are homogeneously anchored on wrinkled and folded GA. High-magnification images (Figure 3d,f) demonstrate that the particle size of amorphous SnO_2 is much smaller than that of crystalline SnO_2. Basically, the XPS and FTIR results illustrate that c-SnO_2/GA show less oxygen-containing groups compared to a-SnO_2/GA, which may probably weaken the bonding strength between SnO_2 and GA, resulting in the aggregation and increscent particle size of crystalline SnO_2. Additionally, as seen in Figure S4 (Supporting Information), the elemental mapping images of a-SnO_2/GA reveal that Sn, O, and C are uniformly distributed in the products.

High-resolution transmission electron microscopy (HRTEM) clearly distinguished the difference between c-SnO_2/GA and a-SnO_2/GA. The obvious basal spaces in Figure S5b (see Supporting Information) and the absence of lattice fringing in Figure S5d (see Supporting Information) well match our design of crystalline and amorphous SnO_2/GA. To further confirm this point, high-angle annular dark-field (HAADF) STEM images and selected area diffraction (SAED) patterns of c-SnO_2/GA and a-SnO_2/GA were carried out. Aberration-corrected STEM images (**Figure 4**a,b) reveal the uniform distribution of SnO_2 on GA. The continuous lattice fringes of c-SnO_2/GA are clearly observed in Figure 4c, indicating that the SnO_2 particles are well-crystallized in c-SnO_2/GA. In detail, the lattice spacings of 0.336 nm correspond to the (110) plane of rutile SnO_2, and the particle dimensions are in the range of 5–10 nm. Differing from c-SnO_2/GA, a-SnO_2/GA have irregular shapes (no lattice fringing) associated with the amorphous state of the SnO_2 particles (Figure 4d), with a particle size of about 2–4 nm. Simultaneously, it can be seen from the SAED patterns (Figure 4e,f) that c-SnO_2/GA and a-SnO_2/GA exhibit obvious differences due to the crystallinity of SnO_2. Remarkably, Figure 4e illustrates a well-resolved set of concentric rings, which can be identified as rutile-like SnO_2 (JCPDS No. 41–1445), confirming a high degree of crystallinity of SnO_2.[30] Conversely, no diffraction rings present in Figure 4f demonstrates a typical amorphous structure of SnO_2 in the composites. All of these results are in good agreement with the results obtained by XRD and HRTEM.

Cyclic voltammetry (CV) was carried out to investigate the electrochemical behavior of a-SnO_2/GA and c-SnO_2/GA anodes with sodium. **Figure 5**a–c illustrates the initial four CV curves of as-prepared products at a scan rate of 0.1 mV s^{-1} in a voltage range of 0.01 to 3.0 V. It can be seen from Figure 5a that no obvious cathodic and anodic peaks emerge, showing typical characteristics of pristine GA anodes for SIBs. The CV profiles of a-SnO_2/GA and c-SnO_2/GA are similar. Simultaneously, there are obvious differences between the first cycle and longer-term cycling. On one hand, in the first cycle, the cathodic peaks ranging from 1.31 to 0.78 V are associated with the formation of the solid electrolyte interphase (SEI) film on the electrode surface and the electrochemical reaction of SnO_2 with Na forming

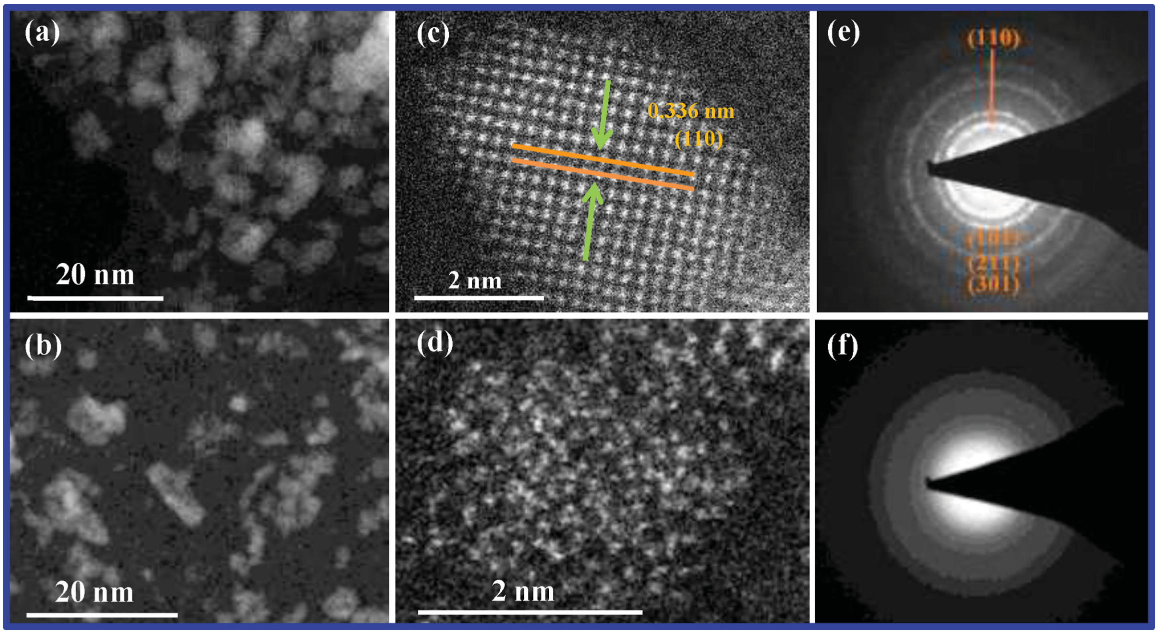

Figure 4. Representative high-angle annular dark-field (HAADF) STEM images, high-resolution HAADF-STEM images, and selected-area diffraction (SAED) patterns of (a,c,e) c-SnO_2/GA and (b,d,f) a-SnO_2/GA, respectively.

Sn and Na_2O which provides the matrix for embedding of Na_xSn alloys,[32] as described by Equation (1). But these peaks disappear in subsequent cycles, indicating that this irreversible reaction only occurs in the initial cycle.[33] On the other hand, two anodic peaks are distinguished at ≈0.23 and 1.5 V, which suggests that the phase transition during the alloying and dealloying processes is more distinctly given by Equation (2).[23] Additionally, all redox peaks remain almost unchanged in the 2nd, 3rd, and 4th cycles, showing good electrochemical reversibility of the SnO_2/GA anodes. Hence, it can be observed that the Na-Sn alloying/de-alloying processes are qualitatively analogous to their Li-Sn counterparts.[21]

Galvanostatic charge–discharge experiments were performed to evaluate the electrochemical performance of the as-prepared products. The charge–discharge curves of pristine GA, a-SnO_2/GA, and c-SnO_2/GA electrodes are shown in Figure 5d–f in the 1st, 2nd, 10th, 50th, and 100th cycles at a current density of 50 mA g^{-1} in a voltage range of 0.01 to 3.0 V. The first discharge capacity of the pristine GA is 349.6 mAh g^{-1}, but the first charge capacity is only 12.4 mAh g^{-1}. In other words, the initial irreversible capacity loss is about 337.2 mAh g^{-1}, which corresponds to a low initial Coulombic efficiency of 3.5%. This indicates that the pristine GA shows very low electrochemical activity as SIB anodes. Meanwhile, the a-SnO_2/GA anode deliver initial discharge and charge capacities of 541.6 and 247.6 mAh g^{-1}, respectively, while the c-SnO_2/GA anode shows lower initial discharge and charge capacities (342.8 and 114.7 mAh g^{-1}, respectively). More strikingly, the discharge and charge capacities of a-SnO_2/GA are higher than those of c-SnO_2/GA upon cycling. Thus, XPS was employed to reveal the chemical state of Sn in the c-SnO_2/GA before and after discharge, as shown in Figure S6 (Supporting Information). Apparently, after discharging to 0.01 V from OCV, the Sn 3d peaks are deconvoluted into two components: (493.0 eV, 484.9 eV) and (494.3 eV, 486.4 eV), and they correspond to Sn^0 and Sn^{2+} states,[34] respectively, indicating that the conversion from SnO_2 to Sn is incomplete. It can explain why the c-SnO_2/GA show a low capacity. In Figure 5e,f, the first discharge profiles show an irreversible plateau at around 1.25 V, which only appears in the first cycle and is likely due to the formation of the SEI film and the irreversible reaction between SnO_2 and Na,[35] as described by Equation (1). In the following charge–discharge processes, no significant capacity fade can be found. This phenomenon agrees well with the results of the CV profiles.

For comaparion, the SnO_2 nanoparticles were synthesized via a facile reflux method (see the Supporting Information for the detailed information). The morphological and structural features of nanoparticle SnO_2 were shown in Figure S7 (Supporting Information), and it can be seen that the particle size is about 15 nm. **Figure 6**a compares the cycling performance of the pristine GA, bare SnO_2, a-SnO_2/GA, and c-SnO_2/GA anodes cycled at a current density of 50 mA g^{-1} (based on the composites mass). As seen clearly, the pristine GA exhibits a low specific capacity of 10 mAh g^{-1} in the 100th cycle. Note that the bare SnO_2 exhibit poor cycle life and it falls to 2 mAh g^{-1} after 100 cycles. As mentioned in the Figure S7 (Supporting Information), the poor performance of SnO_2 anode results from the bigger particle size and large volume change during charge and discharge processes. Interestingly, the cooperation of SnO_2 and GA greatly increased the specific reversible capacity. However, the capacities of the a-SnO_2/GA and c-SnO_2/GA during cycling illustrate different behaviors. The reversible capacity of a-SnO_2/GA continuously decreases from the 1st cycle to the 6th cycle. More importantly, its discharge capacity tends to level off from the 7th cycle to the 100th cycle. The discharge capacity in the 100th cycle accounts for a retention by 91.7% in comparison to that of the 6th cycle. By contrast, the c-SnO_2/GA deliver poor performance with high capacity

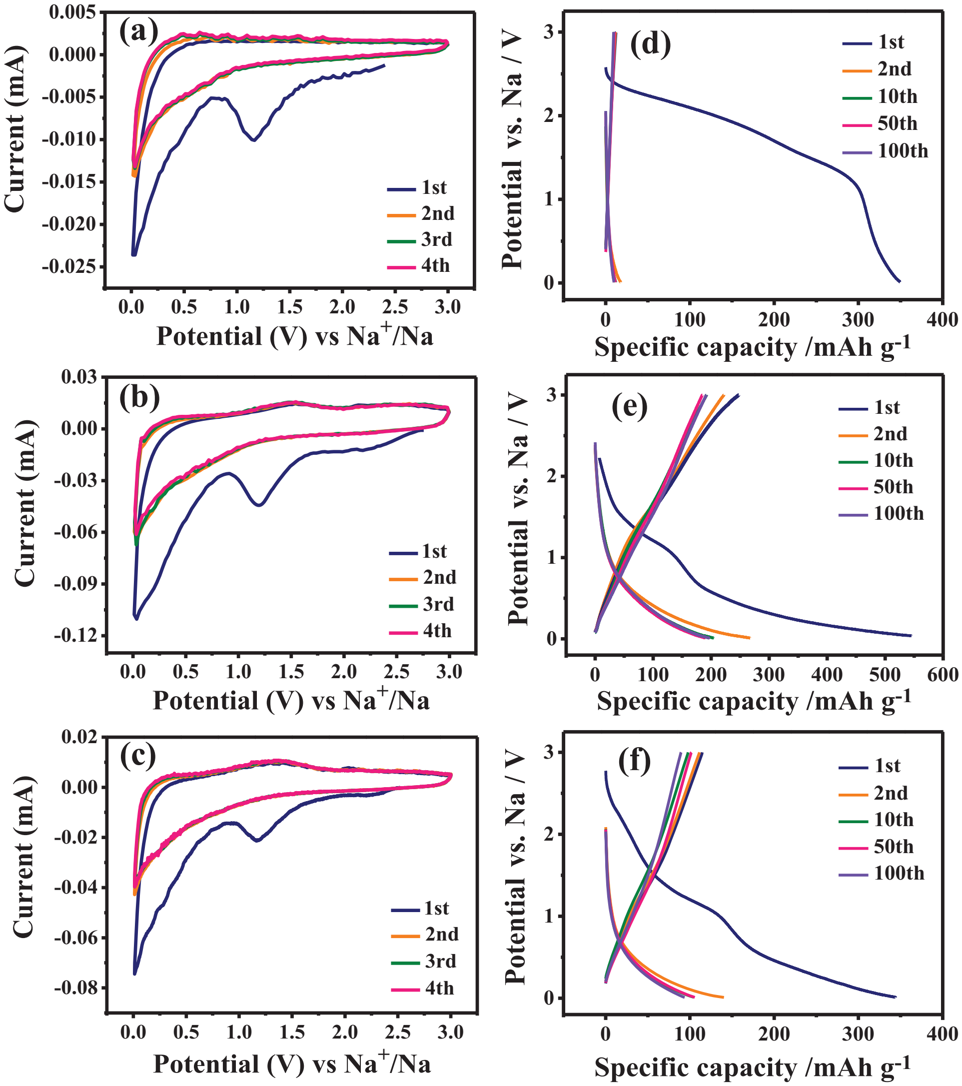

Figure 5. The cyclic voltammetry curves of (a) pristine GA, (b) a-SnO_2/GA, and (c) c-SnO_2/GA at a scan rate of 0.1 mV s^{-1} in the voltage range of 0.01–3.0 V. The discharge/charge profiles of (d) pristine GA, (e) a-SnO_2/GA, and (f) c-SnO_2/GA in the 1st, 2nd, 10th, 50th, and 100th cycles.

fade of 83.0% after 100 cycles compared to 6th cycle. Undoubtedly, the a-SnO_2/GA achieve better cycling performance, originating from the intrinsic isotropic nature and the smaller size of amorphous SnO_2 particles. To highlight the effects of SnO_2 crystallinity on cycling performance, we performed the normalization to remove the effect of GA matrix and compared the specific capacities of amorphous and crystalline SnO_2 (see Figure 6b). It can be seen that the discharge capacity of the amorphous SnO_2 is 380.2 mAh g^{-1} after 100 cycles, which is almost three times as much as 138.6 mAh g^{-1} associated with the crystalline SnO_2. Notably, the cycling performance of both amorphous and crystalline SnO_2 is unstable due to the variable temperature in the testing room. The rate capability of amorphous and crystalline SnO_2 was further studied to confirm the importance of crystallinity, as shown in Figure 6c (see Figure S8 in the Supporting Information for a-SnO_2/GA and c-SnO_2/GA). The amorphous SnO_2 displays an excellent rate capability. It is capable of delivering substantial capacities of 576.2, 274.6, 200, 133.6, and 84.4 mAh g^{-1} at current densities of 50, 100, 200, 400, and 800 mA g^{-1}, respectively. More strikingly, when the current density is reversed back to 50 mA g^{-1} after 76 cycles, a specific discharge capacity of 370.6 mAh g^{-1} is obtained, which is much higher than that of the crystalline SnO_2. Figure 6d compared the discharge capacities of the second cycle at each current density for the amorphous and crystalline SnO_2 anodes. Notably, the amorphous SnO_2 shows superior rate capability compared to crystalline SnO_2. These results clearly confirm that the anode crystallinity results in different cycling performance and rate capability. The amorphous SnO_2 anode can effectively improve SIB performance at various rates, which is a desirable characteristic for high power applications.

To obtain a more thorough insight into the different electrochemical behaviors, electrochemical impedance spectroscopy (EIS) was performed at a charged state of 1.5 V in the 1st, 10th, and 100th cycles, shown in **Figure 7**a,b. Simultaneously, both EIS measurements exhibit two compressed semicircles

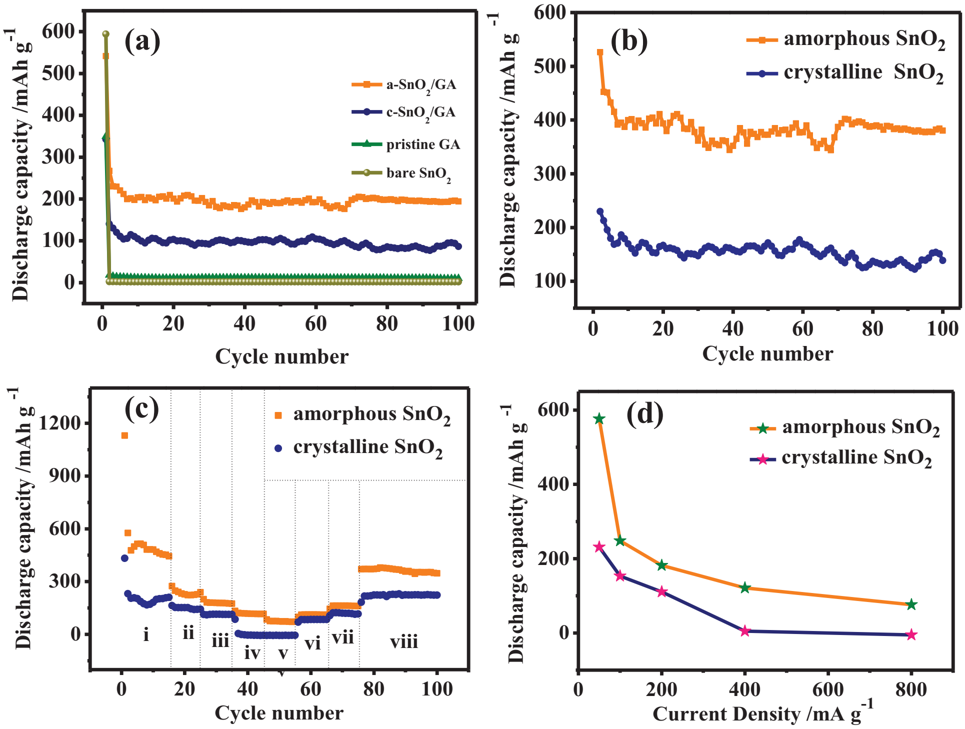

Figure 6. a) Comparison of the cyclic performance of pristine GA, bare SnO_2, a-SnO_2/GA, and c-SnO_2/GA at a current density of 50 mA g^{-1}; b) Cycling performance of amorphous SnO_2 and crystalline SnO_2; c) Rate capability of amorphous SnO_2 and crystalline SnO_2 at various current densities: (i) 50, (ii) 100, (iii) 200, (iv) 400, (v) 800, (vi) 400, (vii) 200, and (viii) 50 mA g^{-1}; d) The capacity retention of amorphous SnO_2 and crystalline SnO_2 at 100, 200, 400, and 800 mA g^{-1} in comparison to the discharge capacity at 50 mA g^{-1}.

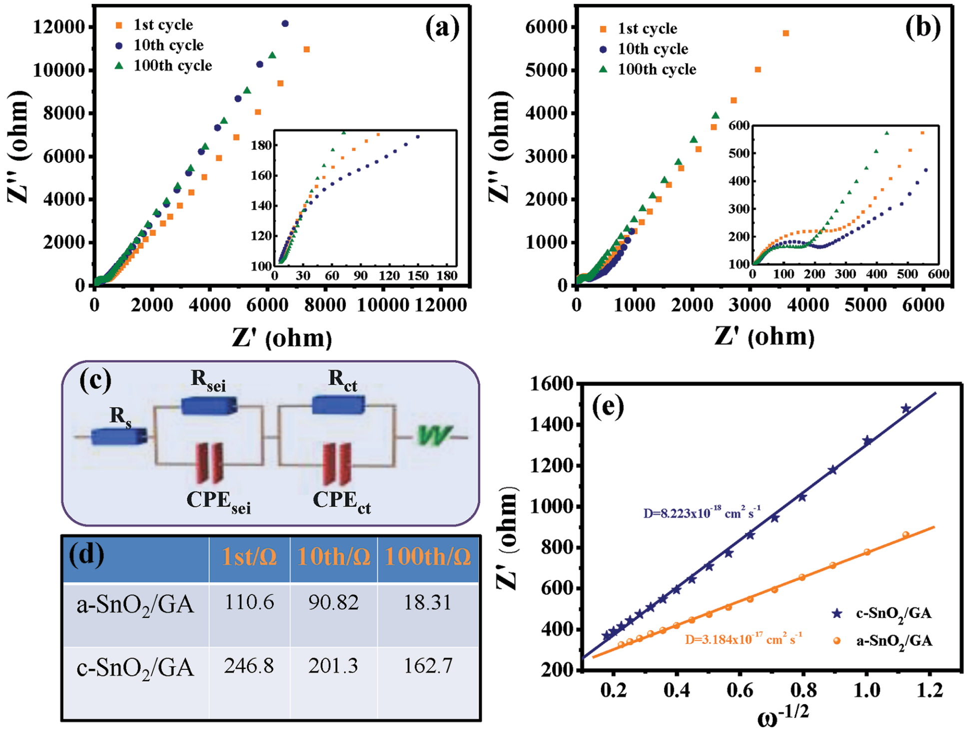

(d)	1st/Ω	10th/Ω	100th/Ω
a-SnO_2/GA	110.6	90.82	18.31
c-SnO_2/GA	246.8	201.3	162.7

Figure 7. The electrochemical impedance spectroscopy of (a) a-SnO_2/GA and (b) c-SnO_2/GA in the 1st, 10th, and 100th cycles; c) The corresponding equivalent circuit used to simulate EIS curves; d) The R_{ct} values of a-SnO_2/GA and c-SnO_2/GA; e) The corresponding plots of the real part of impedance (Z′) as a function of the inverse square root of the angular frequency ($\omega^{-1/2}$) in the Warburg region in the 1st cycle.

followed by a linear section. It can be seen that a-SnO_2/GA have low impedance values compared to c-SnO_2/GA. The EIS curves were fitted by an equivalent circuit (see Figure 7c).[36] In the equivalent circuit, R_s denotes electrolyte ohmic resistance, and Z_w is Warburg resistance originating from the diffusion of Na^+ in the electrode bulk as depicted in the low frequency region of the sloping line.[37] The two depressed semicircles observed at high and medium frequencies are related to the resistance (R_{sei}) and constant phase elements (CPE_{sei}) of the SEI film, as well as the charge transfer resistance (R_{ct}) and constant phase elements (CPE_{ct}) of the electrode, respectively.[2,29,38] The R_{ct} can be strongly influenced by cycling mainly due to the enlarging polarization of the electrode during long cycle times.[39] As shown in Figure 7d, the R_{ct} values of a-SnO_2/GA in the 1st, 10th, and 100th cycles are 110.6, 90.82, and 18.31 Ω, while the values of c-SnO_2/GA are 246.8, 201.3, and 162.7 Ω, respectively. Thus, it can be seen that the c-SnO_2/GA show higher charge transfer resistances than a-SnO_2/GA. In addition, with increasing cycles, the R_{ct} values of both a-SnO_2/GA and c-SnO_2/GA continually decreased, mainly due to the reduction of SnO_2 to metallic Sn. Since the sodium insertion and extraction reaction rates are governed by Na^+ diffusion and electron conductivity, the increased electronic conductivity resulting from formation of metallic Sn during the first cycle would be beneficial for reducing the R_{ct}, indicating enhanced Na^+ electrochemical kinetics.[40] More significantly, the sufficient contact between the active material and the electrolyte leads to the enhanced electrode activity and reduced the impedance of R_{ct}.[38] Meanwhile, the decreased R_{ct} illustrate that the SnO_2/GA electrode may probably experience a slow activation process.[41] In the case of R_{sei}, as a result of the slow growth of the SEI film on the electrode surface, the value continued to increase during the charge–discharge cycles.

Based on Equations (3) and (4)

$$D_{Na^+} = R^2T^2/2n^4F^4\sigma_{\mathrm{w}^2}A^2C^2 \tag{3}$$

$$Z' = R + \sigma_{\mathrm{w}}\omega^{-1/2} \tag{4}$$

EIS was employed to calculate the Na^+ transfer coefficient to better study the effect of crystallinity for sodium storage performance. In Equations (3) and (4), R, T, n, F, A, C, and σ_w are the gas constant, the absolute temperature, the number of electrons per molecule during oxidation, the Faraday's constant, the surface area of the electrode, the Na^+ concentration in the electrode material, and the Warburg coefficient, respectively.[42] The results are shown in Figure 7e. Using Equations (3) and (4), it can be estimated that the sodium diffusion coefficient of the a-SnO_2/GA is 3.184×10^{-17} $cm^2\ s^{-1}$ which is almost 3.8 times as much as 8.223×10^{-18} $cm^2\ s^{-1}$ associated with the c-SnO_2/GA. The enhanced Na^+ diffusion coefficient of a-SnO_2/GA may be attributed to the intrinsically isotropic nature of amorphous materials. To further investigate the kinetics of sodium insertion/extraction into/from the electrode, a series of CV curves with various scan rates of 0.1, 0.2, 0.4, 0.6, and 0.8 mV s^{-1} were recorded to study the Na^+ diffusion coefficient of a-SnO_2/GA and c-SnO_2/GA. In **Figure 8**, one can see that an increase of scan rate causes a progressive shift of the anodic peaks to higher potential as well as an increase in

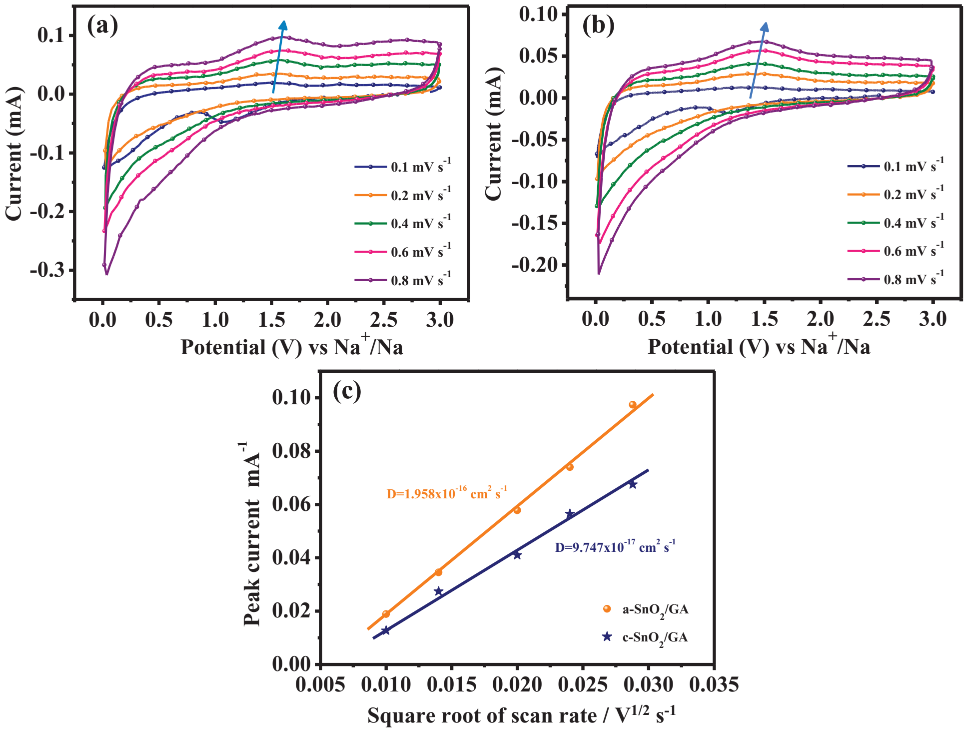

Figure 8. The CV curves in the potential range of 0.01–3.0 V at scanning rates of 0.1, 0.2, 0.4, 0.6, and 0.8 mV s^{-1} for (a) a-SnO_2/GA and (b) c-SnO_2/GA; c) The relationship between I_p and $\nu^{1/2}$ for a-SnO_2/GA and c-SnO_2/GA.

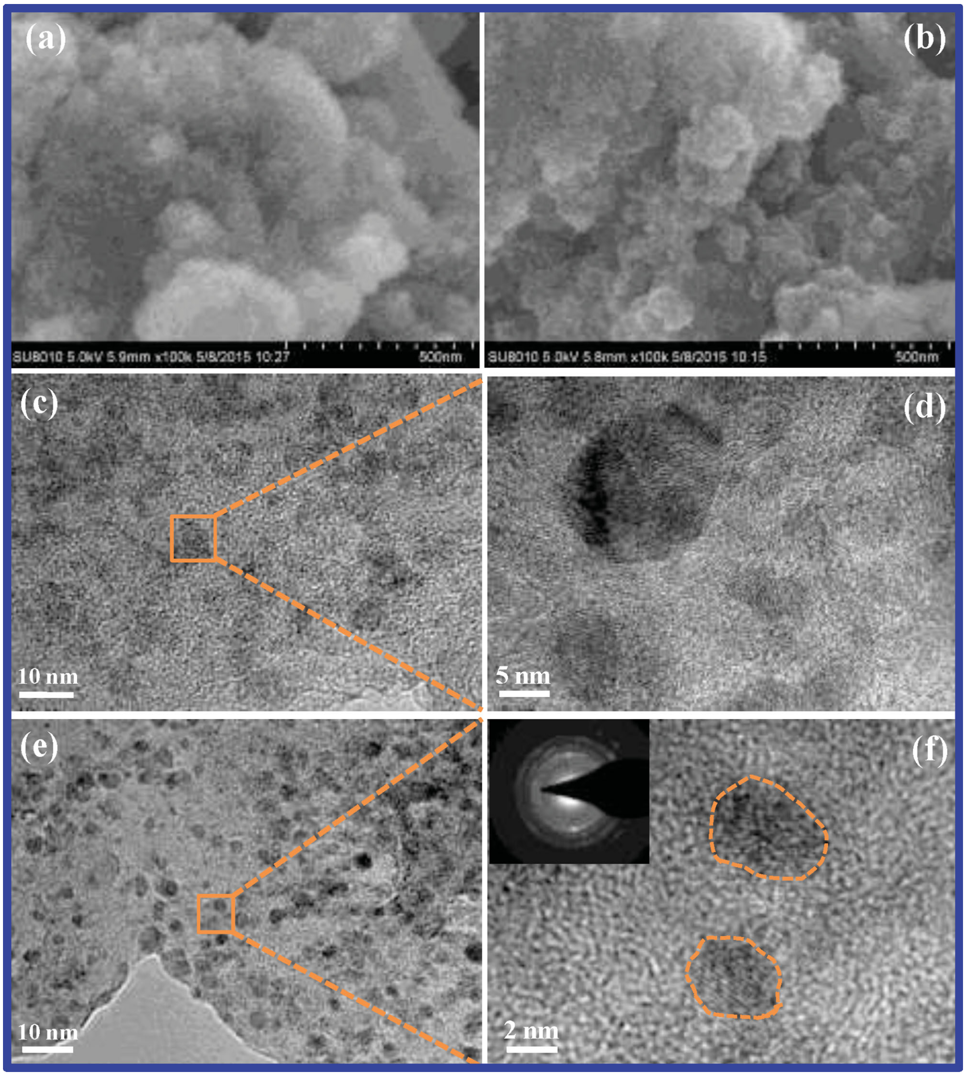

Figure 9. Typical SEM images of (a) c-SnO_2/GA and (b) a-SnO_2/GA after 100 charge/discharge cycles; TEM, HRTEM images of (c,d) c-SnO_2/GA and (e,f) a-SnO_2/GA after 100 cycles, respectively. The inset in (f) is the SAED pattern of cycled a-SnO_2/GA.

peak height. Meanwhile, the linear relationship between I_p and $v^{1/2}$ indicates that the reaction kinetics is controlled by the Na^+ diffusion process.[15c,43] The Na^+ coefficient is evaluated by the Randles–Sevcik equation[44]

$$I_p = 2.69 \times 10^5 n^{3/2} A D^{1/2} v^{1/2} C_0 \quad (5)$$

where I_p is the peak current, n is the charge–transfer number, A is the geometric area of electrode, C_0 is the concentration of Na^+ in the solution, v is the potential scan rate, and D is the diffusion coefficient of Na^+. According to Equation (5), the Na^+ diffusion coefficients of a-SnO_2/GA and c-SnO_2/GA are estimated as 1.958×10^{-16} and 9.747×10^{-17} cm^2 s^{-1}, respectively. It can be calculated that the Na^+ diffusion coefficient of a-SnO_2/GA is two times higher than that of c-SnO_2/GA. The high diffusion coefficient explains why a-SnO_2/GA could exhibit a better sodium storage performance.

Long-term cyclability has been crucial but challenging for rechargeable SIBs, due to the difficulty in alloying/dealloying of the large sodium ions.[45] In this regard, large volume change inevitably occurs upon cycling, resulting in the morphology change of the anodes. The morphologies of cycled c-SnO_2/GA and a-SnO_2/GA anodes after 100 cycles were observed by SEM and TEM. **Figure 9**a,b present SEM images of the aforementioned products. In comparison to the pristine morphology before cycling, one can see from Figure 9a that crystalline SnO_2 particles are seriously pulverized to smaller particles due to the strong volume expansion/contraction upon cycling.[46] This pulverization causes loss of electrical contact between the SnO_2 and GA or conductive agent. As a result, the utilization efficiency of the active materials greatly decreases, which leads to the poor performance of SIBs. By contrast, the pulverization of amorphous SnO_2 seems weaker compared with that of crystalline SnO_2/GA (see Figure 9b). Furthermore, the TEM images in Figure 9c,d show the structure of the c-SnO_2/GA after 100 cycles. Apparently, under the stresses caused by large volume changes, it is possible that some crystalline SnO_2 particles are pulverized. At the same time, particle aggregation

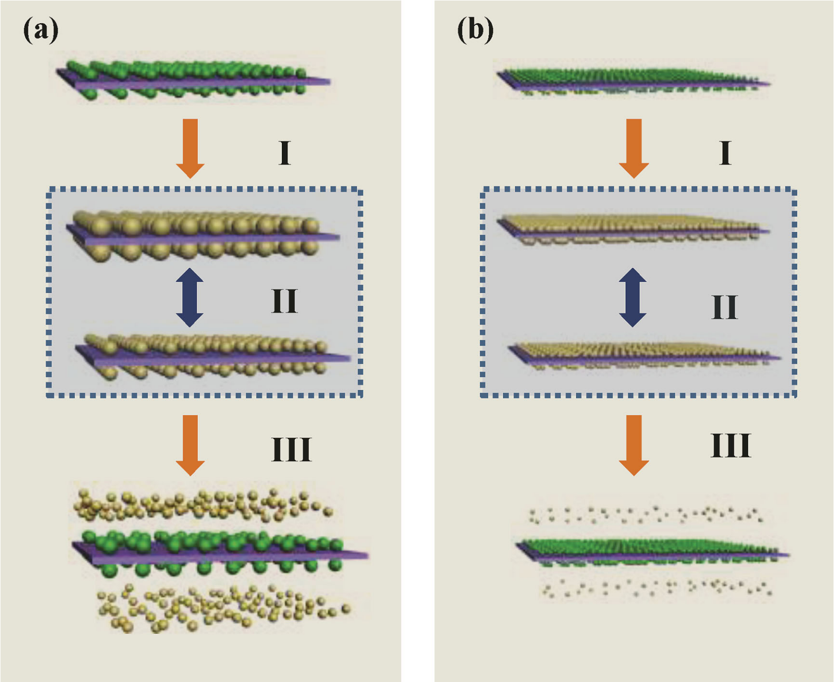

Scheme 1. The morphological evolution of (a) c-SnO_2/GA and (b) a-SnO_2/GA as the anodes in the charge/discharge cycles: (I) the first discharge, pristine SnO_2/GA transform into Na_xSn/GA, (II) the subsequent charge and discharge processes, alloying and dealloying of Na_xSn, and (III) with increased cycling number, some active materials lose their electrical contact with the GA matrix.

of cycled crystalline SnO_2 occurs. As shown in Figure 9e,f, the TEM images of cycled a-SnO_2/GA reveal that particles are homogeneously distributed in the GA, and the HRTEM image further confirms that the dimensions of the particles are in the range of 4–5 nm. Intriguingly, some particles showing clear lattice fringes are observed. Meanwhile, the corresponding SAED (inset of Figure 9f) exhibits a well-resolved set of concentric rings. Both indicate that the resultant particles are substantially crystalline.

The schematic diagram representing the morphological evolution of c-SnO_2/GA and a-SnO_2/GA anodes during the charge/discharge cycles is presented in **Scheme 1**. The conductive matrix GA can relieve SnO_2 volume changes during charge/discharge cycles to some extent,[20] however, the pulverization of particles is inevitable due to large volume expansion and contraction upon cycling. With increased cycling number, however, less active material of the a-SnO_2/GA lose electrical contact with the matrix compared to c-SnO_2/GA due to the isotropic nature of the amorphous SnO_2 (as illustrated in Scheme 1b). Therefore, the performance improvement of amorphous SnO_2 is due to several aspects: (a) intrinsic isotropic nature could effectively better function to relieve the volume expansion/shrinkage upon cycling;[47] (b) the enhanced Na^+ diffusion coefficient of amorphous SnO_2 is about two times higher than that of crystalline SnO_2; and (c) a-SnO_2/GA exhibit more oxygen-containing groups, and the bonding may be easily formed between amorphous SnO_2 and GA. The strong interaction resulting from the bonding could mitigate the elctrical contact loss of the anode material with GA matrix. The cycling performance of the anodes may benefit from some functional groups on the matrix. In addition, amorphous SnO_2 particles with the smaller size demonstrate better function to relieve the volume expansion/shrinkage and make less active material lose electrical contact with the matrix. As a consequence, the a-SnO_2/GA electrode exhibits a better cycling performance and rate capability in SIBs.

As discussed above, a-SnO_2/GA showed superior capacity retention upon cycling. However, relatively low specific capacity was observed due to the low mass loading of SnO_2 (50.7%, a-SnO_2/GA-I) in the composites. To address this disadvantage, we further explored higher mass loading of SnO_2 particles (90.5%, a-SnO_2/GA-II) to improve the sodium–ion storage performance, as shown in **Figure 10**a. Remarkably, by increasing the mass loading of SnO_2, the electrochemical performance of the a-SnO_2/GA-II is significantly improved, as shown in Figure 10b,c (based on the composites mass): (1) they maintain a reversible capacity of 297.4 mAh g^{-1} after 70 cycles, which is higher than a-SnO_2/GA-I (177.8 mAh g^{-1}) (Figure 10b). (2) In terms of the rate performance, a-SnO_2/GA-II exhibits enhanced discharge capacities of 388.3, 312.2, 262.9, 201.4, and 168.8 mAh g^{-1} at current densities of 50, 100, 200, 400, and 800 mA g^{-1}, respectively. The capacity recovers to 291.2 mAh g^{-1} when the current density returns to 50 mA g^{-1} (Figure 10c). (3) As described in Figure 10d, the a-SnO_2/GA-II anodes sustain high capacity retention at current densities of 50, 100, 200, 400, and 800 mA g^{-1}. All results clearly demonstrate that the facile design of a-SnO_2/GA anodes significantly increases the performance of SIBs.

3. Conclusions

In summary, amorphous and crystalline SnO_2/GA were successfully synthesized as anode materials for SIBs. For the first time, this study reported the significant impacts of SnO_2 crystallinity on sodium storage performance. Our results clearly show that amorphous SnO_2 delivers an improved specific capacity, cycling stability, and superior rate capability compared to crystalline SnO_2. For instance, the discharge capacity of the amorphous SnO_2 is 380.2 mAh g^{-1} after 100 cycles, which is almost three times as much as 138.6 mAh g^{-1} associated with the crystalline SnO_2. Furthermore, the a-SnO_2/GA exhibits a high capacity retention of 91.7% relative to the 6th cycle over 100 cycles. By contrast, the crystalline SnO_2/GA delivers poor performance with high capacity fade of 83.0% after 100 cycles compared to 6th cycle. Additionally, the sodium diffusion coefficient of the amorphous SnO_2 is almost two times higher than that of crystalline SnO_2. These results demonstrate that the anode crystallinity strongly affects SIB performance. More signicantly, the impressive electrochemical performance of a-SnO_2/GA could

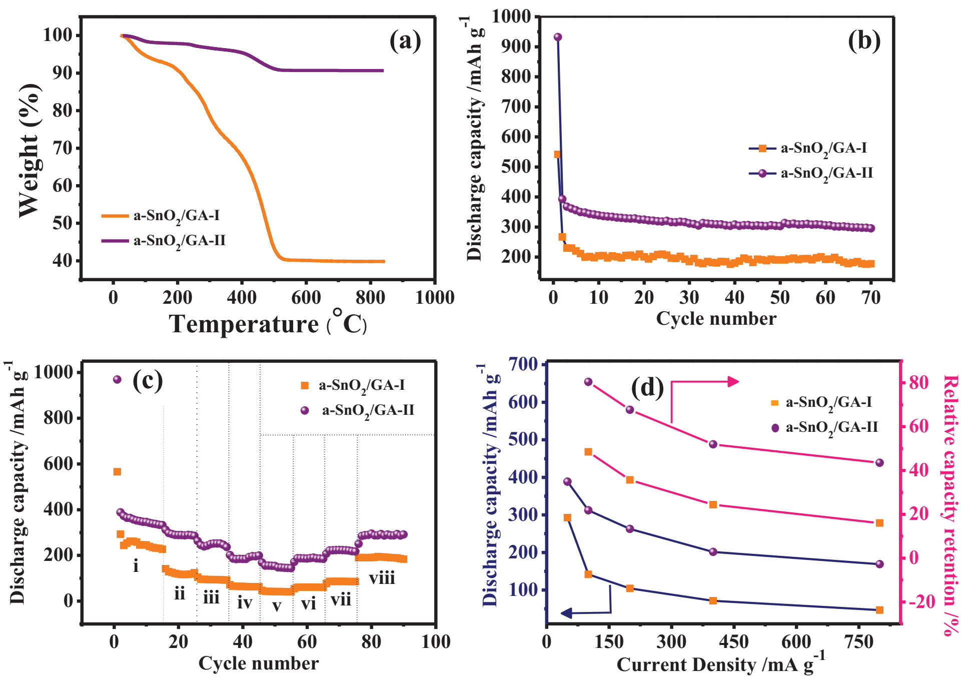

Figure 10. a) TGA curves of a-SnO$_2$/GA-I and a-SnO$_2$/GA-II; b) Comparison of the cyclic performance of a-SnO$_2$/GA-I and a-SnO$_2$/GA-II at a current density of 50 mA g^{-1}; c) Rate capability of a-SnO$_2$/GA-I and a-SnO$_2$/GA-II at various current densities: (i) 50, (ii) 100, (iii) 200, (iv) 400, (v) 800, (vi) 400, (vii) 200, and (viii) 50 mA g^{-1}; d) The capacity retention of a-SnO$_2$/GA-I and a-SnO$_2$/GA-II at 100, 200, 400, and 800 mA g^{-1} in comparison to the discharge capacity at 50 mA g^{-1}.

be attributed to the intrinsic isotropic nature, the enhanced Na$^+$ diffusion coefficient, and the strong interaction between amorphous SnO$_2$ and GA. In addition, amorphous SnO$_2$ particles with the smaller size better function to relieve the volume expansion/shrinkage. Consequently, our study provides an important direction for the design of electrode materials with large volume changes for SIBs. Moreover, the facile synthesis of amorphous SnO$_2$/GA might be one of the most promising strategies for high-performance SIB anode materials.

4. Experimental Section

Synthesis of the a-SnO$_2$/GA and c-SnO$_2$/GA: Graphite oxide (GO) was synthesized by a modified Hummer's method using natural graphite powder as the starting material, which has been reported in our previous work.[48] In a typical synthesis of the composites, 60 mg SnCl$_2$·2H$_2$O (Tianjin Fengchuan Chemical Reagent Science And Technology Co., Ltd. ≥ 98.0%) was first dispersed in 60 mL ethylene glycol (Tianjin Jiangtian Chemical Technology Co., Ltd.) under vigorous magnetic stirring for 1 h. Meanwhile, 39 mg GO was dispersed in 60 mL ethylene glycol by ultrasonication. After 25 min of ultrasonic treatment, the GO suspension in ethylene glycol was added slowly into the above solution using a peristaltic pump to form a homogeneous mixture. Subsequently, the resultant suspension was transferred to three 50 mL Teflon-lined autoclaves and maintained in an oven at 160 °C for 1.5 h. After the autoclave was cooled down, the products were separated and washed with ethanol and water several times via centrifugation and then freeze-dried. The resultant product was the a-SnO$_2$/GA. Subsequently, the product was annealed at 400 °C for 4 h under an argon atmosphere, and the c-SnO$_2$/GA were obtained. In addition, pristine GA was synthesized via a similar method without SnCl$_2$·2H$_2$O.

Physical Characterization: The microstructures of the as-prepared products were investigated by X-ray diffraction (XRD, DX-2700) with Cu-Kα radiation at a scanning rate of 8° min^{-1}. Raman spectra were recorded using a LabRAM HR800. The thermal properties of as-prepared products were characterized via thermogravimetric analysis (TGA, Pyris Diamond6000 TG/DTA, PerkinElmer Co, America) in air over a temperature range of 25–840 °C. The chemical compositions and surface element states of the samples were carried out by X-ray photoelectron spectroscopy (XPS, VG ESCALAB MK II). The structural morphologies of the synthesized composites were examined by scanning electron microscopy (SEM, SU8010, Hitachi) coupled with energy-dispersive spectroscopy (EDS), and by transmission electron microscopy (TEM, JEOL JEM-3000F). In particular, the morphologies of the cycled products were characterized by using a vacuum transfer box to move the samples to the above-mentioned SEM. Aberration-corrected scanning transmission electron microscopy (STEM) was performed using a JEOL ARM200F (JEOL, Tokyo, Japan) transmission electron microscope operated at 200 keV. The microscope was equipped with a CEOS (CEOS, Heidelberg, Germany) probe aberration corrector.

Electrochemical Performance: The composite electrodes consisted of 70% active material, 20% conductive carbon black, and 10% polyvinylidene fluoride (PVDF) by weight, and were prepared by casting the mixture on copper foil. Subsequently, they were dried in a vacuum oven at 80 °C overnight. Subsequently, the electrodes were punched into 12 mm diameter disks and the mass loading of the active material was about 0.44 mg cm^{-2}. The electrolyte used was 1 M NaClO$_4$ in a mixture of ethylene carbonate (EC) and propylene carbonate (PC) (2:1 by volume) with a 10 vol% addition of fluoroethylene carbonate (FEC). The testing cell contained the working electrode, sodium metal as the counter and reference electrodes, and a glass fibre (GF/F, Whatman) as the separator. Electrochemical performance was evaluated using a CR2032-type coin cell assembled in an argon-filled glove box where both the moisture and oxygen concentrations were below 0.1 ppm. The charge–discharge characteristics were measured at a current density of 50 mA g^{-1} in fixed voltage limits of 0.01 to 3.0 V via a multichannel Land battery test system (LANHE CT2001A). The rate capability tests were performed at 50, 100, 200, 400, and 800 mA g^{-1} in the same voltage range. Cyclic voltammetry (CV) tests were carried out with a Princeton Applied Research VersaSTAT4 at a scan rate of 0.1 mV s^{-1} within the potential range of 0.01–3.0 V. Electrochemical impedance spectroscopy was performed from 100 kHz to 0.01 Hz at an amplitude of 5 mV with the Princeton Applied Research VersaSTAT4.

Supporting Information

Supporting Information is available from the Wiley Online Library or from the author.

Acknowledgements

This research was supported by the National Natural Science Foundation of China (Grant No. 51572194), the Key Projects of Tianjin Municipal Natural Science Foundation of China (Grant Nos. 14JCZDJC32200 and 13JCZDJC33900), LPMT (Laboratory of Precision Manufacturing Technology), CAEP (China Academy of Engineering Physics) (Grant No. KF14006), Academic Innovation Funding of Tianjin Normal University (Grant No. 52XC1404), Training Plan of Leader Talent of University in Tianjin, Scientific Research Foundation for Returned Overseas Chinese Scholars of State Education Ministry, and the program of Thousand Youth Talents in Tianjin of China. XS and SL thank support from the Natural Science and Engineering Research Council of Canada and the Canada Research Chair Program.

Received: October 19, 2015
Revised: December 14, 2015

---

[1] a) M. Dirican, M. Yanilmaz, K. Fu, Y. Lu, H. Kizil, X. Zhang, *J. Power Sources* **2014**, *264*, 240; b) K. Fu, L. Xue, O. Yildiz, S. Li, H. Lee, Y. Li, G. Xu, L. Zhou, P. D. Bradford, X. Zhang, *Nano Energy* **2013**, *2*, 976.

[2] Q. Zhou, L. Liu, J. Tan, Z. Yan, Z. Huang, X. Wang, *J. Power Sources* **2015**, *283*, 243.

[3] Y. Wen, K. He, Y. Zhu, F. Han, Y. Xu, I. Matsuda, Y. Ishii, J. Cumings, C. Wang, *Nat. Commun.* **2014**, *5*, 4033.

[4] a) S. W. Kim, D. H. Seo, X. H. Ma, G. Ceder, K. Kang, *Adv. Energy Mater.* **2012**, *2*, 710; b) X. Xie, K. Kretschmer, J. Zhang, B. Sun, D. Su, G. Wang, *Nano Energy* **2015**, *13*, 208.

[5] Y. Sun, L. Zhao, H. Pan, X. Lu, L. Gu, Y. S. Hu, H. Li, M. Armand, Y. Ikuhara, L. Chen, X. Huang, *Nat. Commun.* **2013**, *4*, 1870.

[6] a) A. S. Nagelberg, W. L. Worrell, *J. Solid State Chem.* **1979**, *29*, 345; b) J. Molenda, C. Delmas, P. Hagenmuller, *Solid State Ionics* **1983**, *9–10*, Part *1*, 431.

[7] A. Langrock, Y. Xu, Y. Liu, S. Ehrman, A. Manivannan, C. Wang, *J. Power Sources* **2013**, *223*, 62.

[8] a) Y. Ge, H. Jiang, K. Fu, C. Zhang, J. Zhu, C. Chen, Y. Lu, Y. Qiu, X. Zhang, *J. Power Sources* **2014**, *272*, 860; b) K. T. Kim, C. Y. Yu, C. S. Yoon, S. J. Kim, Y. K. Sun, S. T. Myung, *Nano Energy* **2015**, *12*, 725.

[9] a) Y. Ge, H. Jiang, J. Zhu, Y. Lu, C. Chen, Y. Hu, Y. Qiu, X. Zhang, *Electrochim. Acta* **2015**, *157*, 142; b) S. M. Oh, J. Y. Hwang, C. S. Yoon, J. Lu, K. Amine, I. Belharouak, Y. K. Sun, *ACS Appl. Mater. Interfaces* **2014**, *6*, 11295.

[10] a) X. Liu, T. Chen, H. Chu, L. Niu, Z. Sun, L. Pan, C. Q. Sun, *Electrochim. Acta* **2015**, *166*, 12; b) Z. J. Zhang, Y. X. Wang, S. L. Chou, H. J. Li, H. K. Liu, J. Z. Wang, *J. Power Sources* **2015**, *280*, 107.

[11] J. Park, J. W. Park, J. H. Han, S. W. Lee, K. Y. Lee, H. S. Ryu, K. W. Kim, G. Wang, J. H. Ahn, H. J. Ahn, *Mater. Res. Bull.* **2014**, *58*, 186.

[12] a) M. Mortazavi, C. Wang, J. Deng, V. B. Shenoy, N. V. Medhekar, *J. Power Sources* **2014**, *268*, 279; b) J. Park, J. S. Kim, J. W. Park, T. H. Nam, K. W. Kim, J. H. Ahn, G. Wang, H. J. Ahn, *Electrochim. Acta* **2013**, *92*, 427.

[13] B. L. Ellis, W. R. M. Makahnouk, Y. Makimura, K. Toghill, L. F. Nazar, *Nat. Mater.* **2007**, *6*, 749.

[14] a) X. Wang, X. Zhou, K. Yao, J. Zhang, Z. Liu, *Carbon* **2011**, *49*, 133; b) J. Liang, W. Wei, D. Zhong, Q. Yang, L. Li, L. Guo, *ACS Appl. Mater. Interfaces* **2012**, *4*, 454; c) X. Zhou, L. J. Wan, Y. G. Guo, *Adv. Mater.* **2013**, *25*, 2152.

[15] a) L. F. Xiao, Y. L. Cao, J. Xiao, W. Wang, L. Kovarik, Z. M. Nie, J. Liu, *Chem. Commun.* **2012**, *48*, 3321; b) Y. Zhang, J. Xie, S. Zhang, P. Zhu, G. Cao, X. Zhao, *Electrochim. Acta* **2015**, *151*, 8; c) Z. Li, J. Ding, H. Wang, K. Cui, T. Stephenson, D. Karpuzov, D. Mitlin, *Nano Energy* **2015**, *15*, 369; d) J. W. Wang, X. H. Liu, S. X. Mao, J. Y. Huang, *Nano Lett.* **2012**, *12*, 5897.

[16] a) S. Yang, W. Yue, J. Zhu, Y. Ren, X. Yang, *Adv. Funct. Mater.* **2013**, *23*, 3570; b) I. A. Courtney, *J. Electrochem. Soc.* **1997**, *144*, 2045.

[17] M. Gu, A. Kushima, Y. Y. Shao, J. G. Zhang, J. Liu, N. D. Browning, J. Li, C. M. Wang, *Nano Lett.* **2013**, *13*, 5203.

[18] a) J. C. Kim, D. W. Kim, *Electrochem. Commun.* **2014**, *46*, 124; b) W. Chen, D. Deng, *Carbon* **2015**, *87*, 70; c) L. K. Pei, Q. Jin, Z. Q. Zhu, Q. Zhao, J. Liang, J. Chen, *Nano Res.* **2015**, *8*, 184.

[19] Y. Shen, X. Wang, H. Hu, M. Jiang, X. Yang, H. Shu, *J. Power Sources* **2015**, *283*, 204.

[20] D. W. Su, H. J. Ahn, G. X. Wang, *Chem. Commun.* **2013**, *49*, 3131.

[21] S. Li, Y. Z. Wang, J. X. Qiu, M. Ling, H. H. Wang, W. Martens, S. Q. Zhang, *RSC Adv.* **2014**, *4*, 50148.

[22] Y. Zhao, X. Li, B. Yan, D. Li, S. Lawes, X. Sun, *J. Power Sources* **2015**, *274*, 869.

[23] Y. X. Wang, Y. G. Lim, M. S. Park, S. L. Chou, J. H. Kim, H. K. Liu, S. X. Dou, Y. J. Kim, *J. Mater. Chem. A* **2014**, *2*, 529.

[24] X. Xie, D. Su, J. Zhang, S. Chen, A. K. Mondal, G. Wang, *Nanoscale* **2015**, *7*, 3164.

[25] X. F. Li, X. B. Meng, J. Liu, D. S. Geng, Y. Zhang, M. N. Banis, Y. L. Li, J. L. Yang, R. Y. Li, X. L. Sun, M. Cai, M. W. Verbrugge, *Adv. Funct. Mater.* **2012**, *22*, 1647.

[26] a) R. Liu, D. Li, C. Wang, N. Li, Q. Li, X. Lü, J. S. Spendelow, G. Wu, *Nano Energy* **2014**, *6*, 73; b) C. Zhang, X. Peng, Z. Guo, C. Cai, Z. Chen, D. Wexler, S. Li, H. Liu, *Carbon* **2012**, *50*, 1897; c) B. Zhao, G. Zhang, J. Song, Y. Jiang, H. Zhuang, P. Liu, T. Fang, *Electrochim. Acta* **2011**, *56*, 7340; d) H. Liu, S. Chen, G. Wang, S. Z. Qiao, *Chem. Euro. J.* **2013**, *19*, 16897.

[27] a) Y. T. Xu, Y. Guo, C. Li, X. Y. Zhou, M. C. Tucker, X. Z. Fu, R. Sun, C. P. Wong, *Nano Energy* **2015**, *11*, 38; b) Q. H. Liang, Y. Shi, W. J. Ma, Z. Li, X. M. Yang, *Phys. Chem.* **2012**, *14*, 15657.

[28] a) Y. G. Zhu, Y. Wang, J. Xie, G. S. Cao, T. J. Zhu, X. Zhao, H. Y. Yang, *Electrochim. Acta* **2015**, *154*, 338; b) X. Liu, X. Zhong, Z. Yang, F. Pan, L. Gu, Y. Yu, *Electrochim. Acta* **2015**, *152*, 178; c) A. N. Gildea, D. Wang, G. G. Botte, *J. Appl. Electrochem.* **2015**, *45*, 217.

[29] C. Tan, J. Cao, A. M. Khattak, F. Cai, B. Jiang, G. Yang, S. Hu, *J. Power Sources* **2014**, *270*, 28.

[30] a) H. J. Shin, K. K. Kim, A. Benayad, S. M. Yoon, H. K. Park, I. S. Jung, M. H. Jin, H. K. Jeong, J. M. Kim, J. Y. Choi, Y. H. Lee, *Adv. Funct. Mater.* **2009**, *19*, 1987; b) Z. R. Yue, W. Jiang, L. Wang, S. D. Gardner, C. U. Pittman, *Carbon* **1999**, *37*, 1785.

[31] a) D. Xiong, X. Li, H. Shan, Y. Zhao, L. Dong, H. Xu, X. Zhang, D. Li, X. Sun, *Electrochim. Acta* **2015**, *174*, 762; b) D. Xiong, X. Li,

H. Shan, B. Yan, L. Dong, Y. Cao, D. Li, *J. Mater. Chem. A* **2015**, *3*, 11376.

[32] a) Y. Wang, D. Su, C. Wang, G. Wang, *Electrochem. Commun.* **2013**, *29*, 8; b) X. Xie, S. Chen, B. Sun, C. Y. Wang, G. X. Wang, *ChemSusChem* **2015**, *8*, 2948.

[33] Y. Zhao, J. Li, N. Wang, C. Wu, G. Dong, L. Guan, *J. Phys. Chem. C* **2012**, *116*, 18612.

[34] J. Ding, Z. Li, H. Wang, K. Cui, A. Kohandehghan, X. Tan, D. Karpuzov, D. Mitlin, *J. Mater. Chem. A* **2015**, *3*, 7100.

[35] W. Qin, T. Chen, L. Pan, L. Niu, B. Hu, D. Li, J. Li, Z. Sun, *Electrochim. Acta* **2015**, *153*, 55.

[36] Z. J. Zhang, Q. Y. Zeng, S. L. Chou, X. J. Li, H. J. Li, K. Ozawa, H. K. Liu, J. Z. Wang, *Electrochim. Acta* **2014**, *133*, 570.

[37] W. Song, X. Ji, Z. Wu, Y. Yang, Z. Zhou, F. Li, Q. Chen, C. E. Banks, *J. Power Sources* **2014**, *256*, 258.

[38] B. Yan, M. Li, X. Li, Z. Bai, L. Dong, D. Li, *Electrochim. Acta* **2015**, *164*, 55.

[39] a) D. Wang, X. Li, J. Wang, J. Yang, D. Geng, R. Li, M. Cai, T. K. Sham, X. Sun, *J. Phys. Chem. C* **2012**, *116*, 22149; b) T. Jiang, G. Chen, A. Li, C. Wang, Y. Wei, *J. Alloys Compd.* **2009**, *478*, 604; c) X. Wu, J. Guo, D. Wang, G. Zhong, M. J. McDonald, Y. Yang, *J. Power Sources* **2015**, *281*, 18.

[40] a) G. Xia, N. Li, D. Li, R. Liu, C. Wang, Q. Li, X. Lu, J. S. Spendelow, J. Zhang, G. Wu, *ACS Appl. Mater. Interfaces* **2013**, *5*, 8607; b) F. Ye, B. Zhao, R. Ran, Z. Shao, *Chemistry* **2014**, *20*, 4055.

[41] Y. Li, J. Yao, E. Uchaker, M. Zhang, J. Tian, X. Liu, G. Cao, *J. Phys. Chem. C* **2013**, *117*, 23507.

[42] J. Lin, D. B. Mua, Y. Jin, B. R. Wu, Y. F. Ma, F. Wu, *J. Power Sources* **2013**, *230*, 76.

[43] a) L. Fan, X. Li, Y. Cui, H. Xu, X. Zhang, D. Xiong, B. Yan, Y. Wang, D. Li, *Electrochim. Acta* **2015**, *176*, 610; b) V. Augustyn, J. Come, M. Lowe, J. W. Kim, P. L. Taberna, S. Tolbert, H. Abruña, P. Simon, B. Dunn, *Nat. Mater.* **2013**, *12*, 518.

[44] a) X. Lu, F. Yang, X. Geng, P. Xiao, *Electrochim. Acta* **2014**, *147*, 596; b) S. Zhong, L. Wu, J. Liu, *Electrochim. Acta* **2012**, *74*, 8.

[45] C. Chen, Y. Wen, X. Hu, X. Ji, M. Yan, L. Mai, P. Hu, B. Shan, Y. Huang, *Nat. Commun.* **2015**, *6*, 6929.

[46] L. Liu, M. An, P. Yang, J. Zhang, *Sci. Rep.* **2015**, *5*, 9055.

[47] a) F. Farmakis, C. Elmasides, P. Fanz, M. Hagen, N. Georgoulas, *J. Power Sources* **2015**, *293*, 301; b) M. T. McDowell, S. W. Lee, J. T. Harris, B. A. Korgel, C. Wang, W. D. Nix, Y. Cui, *Nano Lett.* **2013**, *13*, 758.

[48] X. Li, Y. Hu, J. Liu, A. Lushington, R. Li, X. Sun, *Nanoscale* **2013**, *5*, 12607.